Linear and nonlinear optical properties of carbon nanotubes from first-principles calculations

G. Y. Guo* and K. C. Chu
Department of Physics, National Taiwan University, Taipei 106, Taiwan

Ding-sheng Wang
Laboratory for Surface Physics, Institute of Physics, Chinese Academy of Science, Beijing 100080, China

Chun-gang Duan
Department of Physics, University of Nebraska-Omaha, Omaha, Nebraska 68182-0266, USA
(Received 16 October 2003; revised manuscript received 4 March 2004; published 28 May 2004)

A systematic *ab initio* study of the optical as well as structural and electronic properties of the carbon nanotubes within density-functional theory in the local-density approximation has been performed. Highly accurate full-potential projected augmented wave method was used. Specifically, the optical dielectric function ε and second-order optical susceptibility $\chi^{(2)}$ as well as the band structure of a number of the armchair [(3,3),(5,5),(10,10),(15,15),(20,20)], zigzag [(5,0),(10,0),(15,0),(20,0)] and chiral [(4,2),(6,2),(6,4),(8,4), (10,5)] carbon nanotubes have been calculated. The underlying atomic structure of the carbon nanotubes was determined theoretically. It is found that for the electric field parallel to the nanotube axis ($E\|\hat{z}$), the absorptive part ε'' of the optical dielectric function for the small nanotubes (the diameter being smaller than, say, 25 Å) in the low-energy range (0–8 eV) consists of a few distinct peaks. Furthermore, the energy position, the shape, and the number of the peaks depend rather strongly on the diameter and chirality. This suggests that one could use these distinct optical features to characterize the chirality and diameter of the grown nanotubes. In contrast, for the electric field perpendicular to the nanotube axis ($E\perp\hat{z}$), the ε'' spectrum of all the nanotubes studied except the three 4 Å nanotubes in the low-energy region is made up of a broad hump. The bandwidth of the hump increases with the nanotube diameter and the magnitude of the hump is in general about half of that of the ε'' for $E\|\hat{z}$. Surprisingly, given their one-dimensional character, the optical anisotropy of the nanotubes is smaller than that of graphite. For the nanotubes with a moderate diameter (say, 30 Å) such as the (20,20) nanotube, the optical anisotropy is not large and the ε'' spectrum for both electric-field polarizations becomes rather similar to that of graphite with electric-field parallel to the graphene layers ($E\perp c$). The calculated static polarizability $\alpha(0)$ for the semiconducting nanotubes is rather anisotropic with $\alpha(0)$ for $E\|\hat{z}$ being several times larger than that for $E\perp\hat{z}$. For both electric-field polarizations, $\alpha(0)$ is nearly proportional to the square of the tube diameter. The calculated electron energy loss spectra of all the nanotubes studied here for both electric field polarizations are similar to that of $E\perp c$ of graphite, being dominated by a broad $(\pi+\sigma)$-electron plasmon peak at near 27 eV and a small π-electron plasmon peak at 5–7 eV. Only the chiral nanotubes would exhibit second-order nonlinear optical behavior. Furthermore, only two tensor elements $\chi^{(2)}_{xyz}$ and $\chi^{(2)}_{yzx}$ are possibly nonzero with $\chi^{(2)}_{xyz}=-\chi^{(2)}_{yzx}$. For all the chiral nanotubes studied here, both the real and imaginary parts of $\chi^{(2)}_{xyz}(-2\omega,\omega,\omega)$ show an oscillatory behavior. The absolute value of $\chi^{(2)}_{xyz}(-2\omega,\omega,\omega)$ of all the chiral nanotubes in the photon energy range of 0.1–3.0 eV is huge, being up to ten times larger than that of GaAs, suggesting that chiral nanotubes have potential applications in nonlinear optics, e.g., second-harmonic generation and sum-frequency generation. Nevertheless, the static value of both $\chi^{(2)}_{xyz}$ and $\chi^{(2)}_{yzx}$ is zero.

DOI: 10.1103/PhysRevB.69.205416 PACS number(s): 78.67.Ch, 71.20.Tx, 73.22.−f, 42.70.Mp

I. INTRODUCTION

Since their discovery in 1991,[1] carbon nanotubes (CNT's) have attracted considerable interest worldwide because of their unusual properties and great potentials for technological applications. For example, because of their one-dimensional character, metallic CNT's are quantum wires that may exhibit exotic Luttinger-liquid behavior rather than usual Fermi-liquid behavior in normal-metal wires.[2] It was also predicted that nanotori formed from metallic CNT's may exhibit giant paramagnetic moments.[3,4] CNT's can be considered as a layer of graphene sheet rolled up into a cylinder, and the structure of a CNT is completely specified by the chiral vector which is given in term of a pair of integers (n,m).[5] Simple π-band tight-binding model predicts that depending on the way of the rolling up the nanotube can be metallic or semiconducting or insulating.[5] CNT's can be chiral or nonchiral, again depending on the way of the rolling up. CNT's are classified into three types, namely, armchair (n,n) nanotubes, zigzag $(n,0)$ nanotubes, and chiral (n,m) nanotubes with $n\neq m$.[5] Because of one-dimensional character and chirality, chiral CNT's are expected to exhibit a number of unusual optical properties such as optical activity, circular dichroism, and second-harmonic generation.[6–9]

Experimentally, optical properties of CNT's have been studied by the optical ellipsometry,[10] by the electron energy loss spectroscopy,[11] by the reflectivity measurements,[12] and also by the absorption experiments.[13,14] More recently, Bachilo *et al.* reported the spectrofluorimetric measurements on single-walled CNT's.[15] By combining the fluorimetric re-

sults with resonance Raman data, each optical transition was used to identify a specific (n,m) nanotube structure.

Theoretically, Ajiki and Ando investigated, in the effective-mass approximation, the low-energy optical absorption due to interband transitions as a probe of the Aharonov-Bohm effect.[16] Lin and Shung studied, in the π-band model, the frequency dependence of the dielectric functions and discussed a low-energy peak of electron energy loss spectrum.[17] Tasaki *et al.* calculated, again in the π-band model, the optical absorptions, optical rotatory power, and circular dichroism of CNT's.[6] The linear polarizability and third-order nonlinear polarizability have been investigated by Wan *et al.*, who used an extended Hubbard model.[18] The third-order polarizabilities have also been studied by Jiang *et al.*, within the Su-Schrieffer-Heeger model with the Coulomb interaction included.[19]

In spite of these intensive theoretical studies, accurate *ab initio* calculations of the optical properties of CNT's have appeared only very recently[20,21] perhaps because of the heavy demand of the computing resources. π-band model is known to describe well only the electronic excitations around the Fermi level of the large radius CNT's. Accurate *ab initio* calculations of the optical properties are thus needed in order to quantitatively interpret the optical experiments. The chief objectives of the present work are as follows. The first objective is to reveal the optical features of all the three types of the CNT's and their possible dependence on diameter and chirality through a series of *ab initio* calculations. A big challenge in the current CNT research is to grow the CNT's with a specific chirality in a controlled manner and to characterize them. Hopefully, our *ab initio* calculations would help experimental characterization of the CNT's. The second objective is to find out the features and the magnitude of the second-order optical susceptibility of the chiral CNT's in order to see whether they have any potential applications in nonlinear optical devices such as second-harmonic generation and sum-frequency generation.

The rest of this paper is organized as follows. In Sec. II, the theoretical approach and computational details are briefly described. The theoretically determined structural parameters and the curvature energy of the nanotubes are also reported. In Sec. III, the calculated band structure, density of states (DOS), optical dielectric function, and electron energy loss spectrum of graphite, 4 Å nanotubes, armchair nanotubes, zigzag nanotubes, and chiral nanotubes are presented and analyzed in the five subsections, respectively. Only the chiral nanotubes show nonzero second-order optical susceptibility, and thus the calculated second-order optical susceptibilities are presented in Sec. II E. Finally, in Sec. IV, a summary is given.

II. THEORY AND COMPUTATIONAL METHOD

Our *ab initio* calculations for the CNT's were performed using highly accurate full-potential projected augmented wave (PAW) method,[22] as implemented in the VASP package.[23] They are based on density-functional theory with the local-density approximation (LDA). A supercell geometry was adopted so that the nanotubes are aligned in a square array with the closest distance between adjacent nanotubes being at least 6 Å. As a test, calculations with larger intertube distances were performed and no discernable differences were found. A large plane-wave cutoff of 450 eV was used throughout. We consider a few representative CNT's with a small or moderate diameter from all three types, as listed in Table I.

TABLE I. Theoretical structural parameters and curvature energy of the nanotubes studied. D is the average diameter, T is the length of translational vector, N is the number of atoms per unit cell, and E_c is the curvature energy (see text). For comparison, D and T of the ideal nanotubes constructed assuming C-C bond length of 1.415 Å are also listed (in brackets).

	D (Å)	T(Å)	N	E_c (eV/C)
(4,2)	4.25 (4.13)	11.27 (11.23)	56	0.45
(6,2)	5.70 (5.62)	15.36 (15.30)	104	0.24
(6,4)	6.86 (6.80)	18.57 (18.50)	152	0.17
(8,4)	8.30 (8.25)	11.21 (11.23)	112	0.11
(10,5)	10.36 (10.32)	11.21 (11.23)	140	0.07
(5,0)	4.04 (3.90)	4.25 (4.24)	20	0.50
(10,0)	7.85 (7.80)	4.24 (4.24)	40	0.13
(15,0)	11.60 (11.70)	4.24 (4.24)	60	0.06
(20,0)	15.61 (15.60)	4.24 (4.24)	80	0.03
(3,3)	4.11 (4.05)	2.46 (2.45)	12	0.48
(5,5)	6.78 (6.75)	2.45 (2.45)	20	0.17
(10,10)	13.46 (13.51)	2.45 (2.45)	40	0.04
(15,15)	20.25 (20.26)	2.45 (2.45)	60	0.02
(20,20)	26.96 (27.02)	2.45 (2.45)	80	0.01

A. Structural optimization

First, the ideal nanotubes were constructed by rolling up a graphene sheet. Their atomic positions and lattice constants were then fully relaxed by a conjugate gradient technique. Theoretical equilibrium nanotube structures were obtained when the forces acting on all the atoms were less than 0.02 eV/Å. In these atomic structure optimizations, a uniform grid $(1\times1\times n)$ along the nanotube axis (z axis) with the number n of the k points ranging from 12 to 50, was used. The special k-point method plus Gaussian broadening technique was used for the Brillouin-zone integration. The theoretical equilibrium lattice constants and averaged nanotube radii are listed in Table I. Note that for the nanotubes with a moderate diameter ($\geqslant$10 Å), the equilibrium structures are already found to be almost the same as that of the ideal nanotubes constructed by rolling up a graphene sheet with a C-C bondlength of 1.415 Å. This is consistent with the fact that the calculated curvature energy E_c (total energy relative to that of graphene sheet) of the nanotubes with such a diameter is already smaller than 0.1 eV/atom (Table I).

B. Band-structure calculation

The self-consistent electronic band-structure calculations were then carried out for the theoretically determined CNT structures. In these selfconsistent calculations, a denser

k-point grid was used and *n* ranges from 40 to 80. The DOS was evaluated from the self-consistent band structure by Gaussian broadening method, i.e.,

$$N(\epsilon)=\sum_n \sum_{\mathbf{k}} w_{\mathbf{k}}\delta(\epsilon-\epsilon_{\mathbf{k}n}), \tag{1}$$

where the Dirac delta function $\delta(x)$ is approximated by a Gaussian function,

$$\delta(x)\approx \frac{1}{\sqrt{\pi}\Gamma}e^{-x^2/\Gamma^2}, \tag{2}$$

$w_{\mathbf{k}}$ the weight associated with *k*-point $\mathbf{k}$ and $\epsilon_{\mathbf{k}n}$ the *n*th energy band. Here the Gaussian width Γ is set to 0.05 eV. An even denser *k*-point grid along the *z* axis was used ($n \sim 40$–300) for DOS calculations.

C. Calculation of the optical properties

In this work, the optical properties were calculated based on the independent-particle approximation, i.e., the excitonic effects and the local-field corrections were neglected. As has been shown in previous calculations[24] and also below, the dielectric function of graphite calculated within the single-electron picture are in good agreement with experiments. Therefore, it might be expected that the independent-particle approximation could work rather well for the CNT's too.

The imaginary part of the dielectric function $\varepsilon(\omega)$ due to direction interband transitions is given by Fermi golden rule (see, e.g., Ref. 25) (atomic units are used in the rest of this paper), i.e.,

$$\varepsilon''_{aa}(\omega)=\frac{4\pi^2}{\Omega\omega^2}\sum_{i\in VB, j\in CB}\sum_{\mathbf{k}} w_{\mathbf{k}}|p^a_{ij}|^2\delta(\epsilon_{\mathbf{k}j}-\epsilon_{\mathbf{k}i}-\omega), \tag{3}$$

where Ω is the unit-cell volume and ω the photon energy. Also, VB and CB denote the conduction and valence bands, respectively. The dipole transition matrix elements $p^a_{ij}=\langle \mathbf{k}j|\hat{p}_a|\mathbf{k}i\rangle$ were obtained from the self-consistent band structures within the PAW formalism.[26] Here $|\mathbf{k}n\rangle$ is the *n*th Bloch state wave function with crystal momentum $\mathbf{k}$ and *a* denotes the Cartesian components. The real part of the dielectric function is obtained from $\varepsilon''(\omega)$ by a Kramer-Kronig transformation

$$\varepsilon'(\omega)=1+\frac{4}{\pi}\mathbf{P}\int_0^\infty d\omega'\frac{\omega'\varepsilon''(\omega')}{\omega'^2-\omega^2}. \tag{4}$$

Here $\mathbf{P}$ denotes the principal value of the integral. Given the complex dielectric function $(\varepsilon'+i\varepsilon'')$, all other linear optical properties such as refractive index, reflectivity, and absorption spectrum can be calculated. Furthermore, the electron energy loss spectrum at the long-wavelength limit is $-\mathrm{Im}[(\varepsilon'+i\varepsilon'')^{-1}]$ and the electric polarizability α is given by $\varepsilon'(\omega)=1+4\pi\alpha(\omega)/\Omega$.

Following previous nonlinear optical calculations,[27] the imaginary part of the second-order optical susceptibility due to direct interband transitions is given by[28]

$$\chi''^{(2)}_{abc}(-2\omega,\omega,\omega)=\chi''^{(2)}_{abc,VE}(-2\omega,\omega,\omega)+\chi''^{(2)}_{abc,VH}(-2\omega,\omega,\omega), \tag{5}$$

where the contribution due to the so-called virtual-electron (VE) process is

$$\chi''^{(2)}_{abc,VE}=-\frac{\pi}{2\Omega}\sum_{i\in VB}\sum_{j,l\in CB}\sum_{\mathbf{k}} w_{\mathbf{k}}\left\{\frac{\mathrm{Im}[p^a_{jl}\langle p^b_{li}p^c_{ij}\rangle]}{\epsilon^3_{li}(\epsilon_{li}+\epsilon_{ji})}\times\delta(\epsilon_{li}-\omega)-\frac{\mathrm{Im}[p^a_{ij}\langle p^b_{jl}p^c_{li}\rangle]}{\epsilon^3_{li}(2\epsilon_{li}-\epsilon_{ji})}\delta(\epsilon_{li}-\omega)+\frac{16\mathrm{Im}[p^a_{ij}\langle p^b_{jl}p^c_{li}\rangle]}{\epsilon^3_{ji}(2\epsilon^3_{li}-\epsilon^3_{ji})}\delta(\epsilon_{ji}-2\omega)\right\} \tag{6}$$

and that due to the virtual-hole (VH) process

$$\chi''^{(2)}_{abc,VH}=\frac{\pi}{2\Omega}\sum_{i,l\in VB}\sum_{j\in CB}\sum_{\mathbf{k}} w_{\mathbf{k}}\left\{\frac{\mathrm{Im}[p^a_{li}\langle p^b_{ij}p^c_{jl}\rangle]}{\epsilon^3_{jl}(\epsilon_{jl}+\epsilon_{ji})}\times\delta(\epsilon_{jl}-\omega)-\frac{\mathrm{Im}[p^a_{ij}\langle p^b_{jl}p^c_{li}\rangle]}{\epsilon^3_{jl}(2\epsilon_{jl}-\epsilon_{ji})}\delta(\epsilon_{jl}-\omega)+\frac{16\mathrm{Im}[p^a_{ij}\langle p^b_{jl}p^c_{li}\rangle]}{\epsilon^3_{ji}(2\epsilon_{jl}-\epsilon_{ji})}\delta(\epsilon_{ji}-2\omega)\right\}. \tag{7}$$

Here $\epsilon_{ji}=\epsilon_{\mathbf{k}j}-\epsilon_{\mathbf{k}i}$ and $\langle p^b_{jl}p^c_{li}\rangle=\frac{1}{2}(p^b_{jl}p^c_{li}+p^b_{li}p^c_{jl})$. The real part of the second-order optical susceptibility is then obtained from $\chi''^{(2)}_{abc}$ by a Kramer-Kronig transformation

$$\chi'^{(2)}(-2\omega,\omega,\omega)=\frac{2}{\pi}\mathbf{P}\int_0^\infty d\omega'\frac{\omega'\chi''^{(2)}(2\omega',\omega',\omega')}{\omega'^2-\omega^2}. \tag{8}$$

In the present calculations, the δ function in Eqs. (3), (6), and (7) is again approximated by a Gaussian function [Eqs. (2)] with $\Gamma=0.2$ eV. The same *k*-point grid as in the DOS calculation is used. Furthermore, to ensure that ε' and also $\chi'^{(2)}$ calculated via Kramer-Kronig transformation [Eqs. (4) and (9)] are reliable, at least ten energy bands per atom are included in the present optical calculations. The unit-cell volume Ω in Eqs. (3), (6), and (7) is not well-defined for nanotubes. Therefore, like the previous calculations,[21] we used the effective unit-cell volume of the nanotubes rather than the volume of the supercells which is arbitrary. The effective unit-cell of a nanotube is given by $\Omega=\pi[(D/2+d/2)^2-(D/2-d/2)^2]T$, where *d* is the thickness of the nanotube cylinder which is set to the interlayer distance of graphite (3.35 Å, see the following section). *D* and *T* are the diameter and length of translational vector of the nanotube (Table I), respectively.

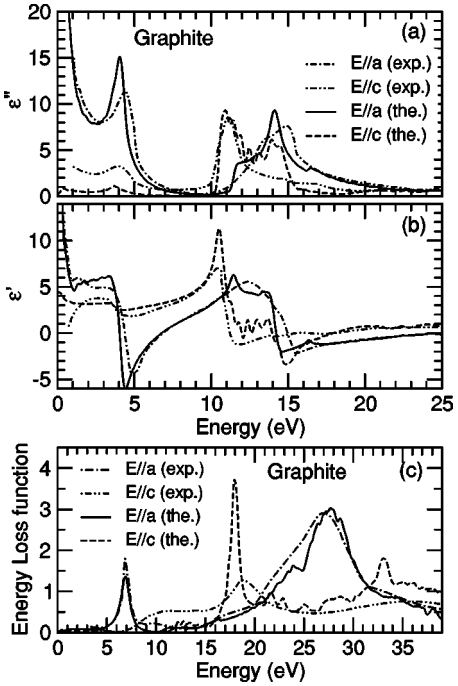

FIG. 1. Theoretical (the) and experimental (exp) (from Ref. 29 and references therein) dielectric function and energy loss function of graphite.

III. RESULTS AND DISCUSSION

A. Graphite and graphene sheet

In order to access the accuracy of the present independent-particle approach to the optical properties of the carbon structures and also for comparison with the CNT's, we first calculated the self-consistent electronic band structure and also linear optical dielectric function for graphite and an isolated graphene sheet. Note that both systems would not show second-order nonlinear optical behavior because they possess inversion symmetry. The isolated graphene sheet is simulated by a slab-supercell approach with an intersheet distance of 6 Å. The theoretically determined lattice constants ($a=2.45$ Å and $c=6.70$ Å for graphite and $a=2.45$ Å for the graphene sheet) were used. Note that the theoretical lattice constants of graphite agree well with the experimental values ($a=2.46$ Å and $c=6.72$ Å).

The calculated optical dielectric function $\varepsilon(\omega)$ and electron energy loss function of graphite are shown in Fig. 1. The calculated $\varepsilon(\omega)$ of the graphene sheet is similar to that of graphite and hence is not plotted here. In the calculations, a k-point grid of $54\times54\times15$ for graphite and $60\times60\times1$ for the graphene sheet is used. The measued $\varepsilon(\omega)$ Ref. 29, and also energy loss function[29] of graphite are also plotted in Fig. 1. The electronic band structure and optical properties of graphite have been extensively studied both experimentally and theoretically (see, e.g., Refs. 24, 29, 30 and references therein), and they are well understood. Nonetheless, here we summarize the main features in the optical spectra which are relevant to the discussions below.

The optical properties of graphite can be conveniently divided into two spectral regions. In the low-energy range from 0 to 9 eV, interband optical transitions involve mainly the π bands which arise from the atomic $2p_z$ orbitals, extending above and below the carbon-layer planes. It is these electrons which play the principal role in the electrical conductivity. At higher energies, a broad peak of optical absorption between 11 and 15 eV [see Fig. 1(a)] is associated with interband transitions involving the three $2s$, $2p_x$, $2p_y$ orbitals, which form the coplanar σ bonds joining one carbon to its three neighors within the layer. Strong anisotropy in the optical spectra can be expected, as demonstrated in Fig. 1, because of distinct optical selection rules. In particular, for a single graphene sheet, only $\pi\rightarrow\pi^*$ and $\sigma\rightarrow\sigma^*$ transitions are allowed if the electric-field vector **E** is polarized parallel to the carbon-layer planes ($E\|\hat{a}$) while in contrast, only $\pi\rightarrow\sigma^*$ and $\sigma\rightarrow\pi^*$ transitions are allowed if the electric-field vector **E** is polarized perpendicular to the carbon-layer planes ($E\|\hat{c}$). This is why there is strong absorption for $E\|\hat{a}$ [Fig. 1(a)]. For the graphene sheet, there is no optical absorption for $E\|\hat{c}$ in the low-energy region (not shown here). The very weak absorption in the low-energy region for $E\|\hat{c}$ in Fig. 1(a) is caused by weak interaction between the graphene layers in graphite.

For $E\|\hat{a}$, two prominant peaks are found in the energy loss function, $-\mathrm{Im}\epsilon^{-1}$ [Fig. 1(c)]. A small one near 6.9 eV has been attributed to the collective excitation of π electrons partially screened by the σ electrons. A large broad resonance near 27.7 eV is associated with plasma oscillations involving both the π and σ electrons. On the other hand, for $E\|\hat{c}$, the peaks near 6.9 and 27.7 eV are completely absent. There is instead a sharp resonance at 18.0 eV and a weaker one near 33.0 eV [Fig. 1(c)].

Clearly, there is an overall good agreement between the calculated and measured dielectric function and energy loss function (Fig. 1), suggesting that the present LDA plus independent-particle approach is perhaps adequate for describing the optical properties of carbon nanostructures such as the nanotubes studied here. Nevertheless, minor differences between the calculated and measured $\varepsilon(\omega)$ do exist, as also found in previous *ab initio* calculations.[24] For example, the calculations predict a rather prominant peak near 14 eV in the $\varepsilon''(\omega)$ for $E\|\hat{c}$ which, however, appears only as a weak shoulder in the corresponding experimental spectrum [Fig. 1(a)]. This discrepancy may or may not be caused by the inadequacy of the LDA because different experiments gave rise to rather different $\varepsilon''(\omega)$ for $E\|\hat{c}$.[29] More accurate measurements are perhaps needed to resolve this problem.

B. 4 Å carbon nanotubes

The calculated energy bands and DOS of the (5,0), (3,3), and (4,2) nanotubes are shown in Fig. 2. All the three nanotubes have a diameter of about 4 Å (Table I). The present *ab initio* calculations show that both (5,0) and (3,3) are metals while (4,2) is a semiconductor with a small gap of 0.26 eV. As mentioned before, these *ab initio* band structures differ significantly from that of simple π-band model. For ex-

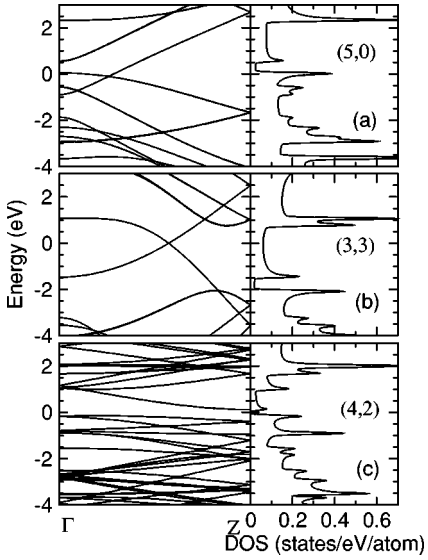

FIG. 2. Energy bands and density of states of the (5,0), (3,3), and (4,2) nanotubes. The Fermi level is at 0 eV.

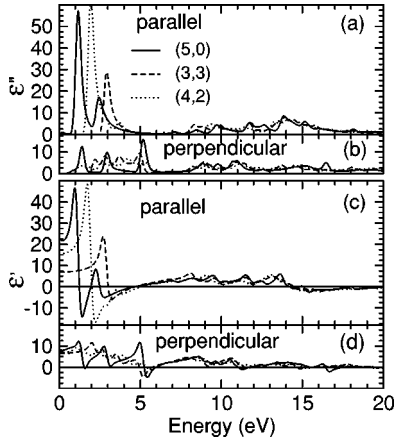

FIG. 3. Calculated dielectric function and energy loss function of the (5,0), (3,3), and (4,2) nanotubes. ''Parallel'' and ''perpendicular'' denote electric fields polarized parallel and perpendicular to the nanotube axis, respectively.

ample, simple π-band model would predict the (5,0) and (4,2) nanotubes to be a semiconductor with a band gap of around 2.0 eV. Though π-band model also predicts that (3,3) is a metal, the predicted Fermi wave vector k_F is 0.667 π/T (T is the lattice constant), which is significantly different from the prediction (0.577 π/T)] of the present *ab initio* calculations. These discrepancies between π-band model and *ab initio* calculations are caused by the so-called curvature effects (see, e.g., Ref. 5 and references therein). When a graphene sheet is rolled up to form a nanotube, π and σ orbitals are no longer orthogonal to each other and they now can hybridize. This hybridization of the π and σ orbitals would modify the band structure predicted by π-band model. The smaller the nanotubes, the larger the curvature and the larger the hybridization. The 4 Å nanotubes studied here are the smallest carbon nanotubes ever reported so far,[14] and thus have the strongest curvature effects. It is gratifying that the present energy bands and DOS for the three nanotubes are almost identical to that of recent *ab initio* calculations.[20,21]

The calculated ε' and ε'' of the (5,0), (3,3), and (4,2) nanotubes are displayed in Fig. 3. Strikingly, the dielectric function (Fig. 3) is very different from that of graphite (Fig. 1). In particular, the absorptive part ε'' in the low-energy range from 0 to 8 eV is several times larger than in the high-energy range from 8 eV to 20 eV. For the electric field parallel to the nanotube axis ($E\|\hat{z}$), the ε'' spectrum in the low-energy region is dominated by a single or double peak [Fig. 3(a) and Table II]. Therefore the distinct features observed in recent optical-absorption measurements[14] could be interpreted. Specifically, feature *A* at 1.4 eV, *B* at 2.1 eV, and *C* at 3.1 eV from the experiments[14] could be assigned to the peak at 1.2 eV for (5,0), at 2.0 eV (4,2), and at 2.9 eV for (3,3) (Table II), respectively. Clearly, the theoretical energy positions are up to 15% smaller than the corresponding measured values. Nevertheless, we consider this level of agreement between the calculations and the measurements as being satisfactory, given the fact that LDA generally underestimates band gaps and electronic excitation energies by more than 10%. Also, in this low-energy region, the optical anisotropy is remarkable [Figs. 3(b) and 3(d)]. However, the experiments[14] indicate a much stronger optical anisotropy. In particular, for the electric field perpendicular to the tube axis ($E\perp\hat{z}$), the measured absorption is small and flat. This marked discrepancy between the present calculations and the experiments is due to the well-known screening of the electric field perpendicular to the nanotube axis (the depolarization effect).[16,31] This depolarization effect does not allow direct comparison of the present calculations with optical experiments for $E\perp\hat{z}$.

It is noted that the present dielectric function for all the three nanotubes is very similar to that of recent *ab initio* calculations.[20,21] In particular, the energy position of the peaks and the shape of the spectra are almost identical. The

TABLE II. Calculated energy positions of the distinct peaks in the ε'' for $E//\hat{z}$ of the nanotubes studied (see text) and also calculated Fermi wave vector k_F of the armchair nanotubes. Note that the ideal k_F value from π-band model is 0.667(π/T) (see text).

	Energy (eV)	k_F (π/T)
(4,2)	2.0	
(6,2)	1.1, 2.7	
(6,4)	1.2, 1.9, 3.4	
(8,4)	0.9, 1.9, 2.7, 3.5	
(10,5)	0.8, 1.3, 2.8, 3.7	
(5,0)	1.2, 2.5	
(10,0)	0.8, 2.5, 3.1	
(15,0)	1.6, 2.1, 3.7	
(20,0)	0.6, 2.1, 2.9, 3.7	
(3,3)	2.9	0.577
(5,5)	2.7, 3.6	0.629
(10,10)	1.6, 2.8, 3.9	0.659
(15,15)	1.1, 2.1, 2.8, 4.0	0.671
(20,20)		0.664

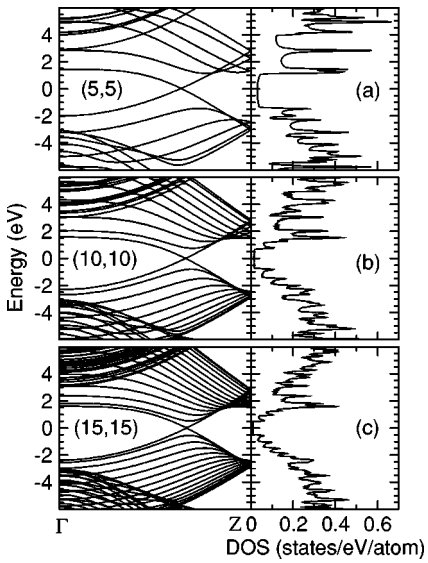

FIG. 4. Energy bands and density of states of the armchair nanotubes. The Fermi level is at 0 eV.

absorption coefficients α have also been calculated and again they are almost the same as that in Ref. 21. Thus, they are not shown here.

C. Band structure of nanotubes

The calculated energy bands and DOS of the armchair [(5,5), (10,10), and (15,15)] nanotubes are shown in Fig. 4. As can be expected from π-band model, all three nanotubes are a metal. The calculated Fermi wave vectors k_F are listed in Table II. The k_F is $0.629(\pi/T)$ for (5,5), $0.659(\pi/T)$ for (10,10), and $0.671(\pi/T)$ for (15,15), respectively. For the (10,10) and (15,15) nanotubes, the calculated k_F is already close to the ideal value of $0.667(\pi/T)$. The (20,20) nanotube has also been calculated and the k_F is $0.664(\pi/T)$.

The calculated energy bands and DOS of the zigzag [(10,0), (15,0), and (20,0)] nanotubes are shown in Fig. 5. As

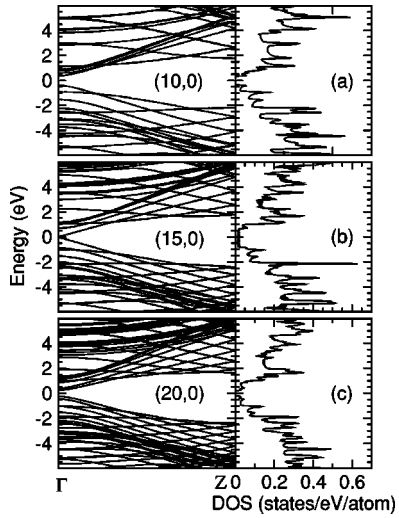

FIG. 5. Energy bands and density of states of the zigzag nanotubes. The Fermi level is at 0 eV.

TABLE III. Calculated band gap E_g, static dielectric constant $\varepsilon(0)$, and polarizability $\alpha(0)$ per unit length for the nonmetallic nanotubes studied in this work.

	E_g (eV)	$\varepsilon_{xx}(0)$ [$\varepsilon_{zz}(0)$]	$\alpha_{xx}(0)$ ($\alpha_{zz}(0)$) [Å^2]
(4,2)	0.26	7.0 (15.4)	21.5 (51.6)
(6,2)	0.67	7.2 (21.9)	29.4 (99.0)
(6,4)	1.09	7.3 (22.1)	36.0 (120.6)
(8,4)	0.81	8.7 (23.6)	53.4 (156.7)
(10,5)	0.74	9.9 (25.3)	77.2 (210.8)
(10,0)	0.40	8.2 (26.8)	47.2 (169.2)
(20,0)	0.14	13.0 (36.1)	156.9 (459.0)

expected, the (10,0) and (20,0) nanotubes are a semiconductor with a band gap of 0.40 and 0.14 eV (Table III), respectively. However, the (15,0) nanotube is predicted to be a narrow-gap (0.025 eV) semiconductor instead of a semimetal from π-band model. Note that this band-gap value is in good agreement with recent scanning tunneling microscopy (STM) measurements.[32]

The calculated energy bands and DOS of the chiral (6,2),(6,4), (8,4), and (10,5) nanotubes are displayed in Fig. 6. All the chiral nanotubes studied here are a semiconductor [Figs. 2 and 6) and their band gaps are listed in Table III.

D. Dielectric constant and static polarizability

Figures 7–9 display, respectively, the calculated ε' and ε'' for the armchair [(5,5), (10,10), (15,15), and (20,20)] nanotubes, the zigzag [(10,0), (15,0), and (20,0)] nanotubes, and the chiral [(6,2), (6,4), (8,4), and (10,5)] nanotubes. The spectra can be divided into two regions, namely, the low-

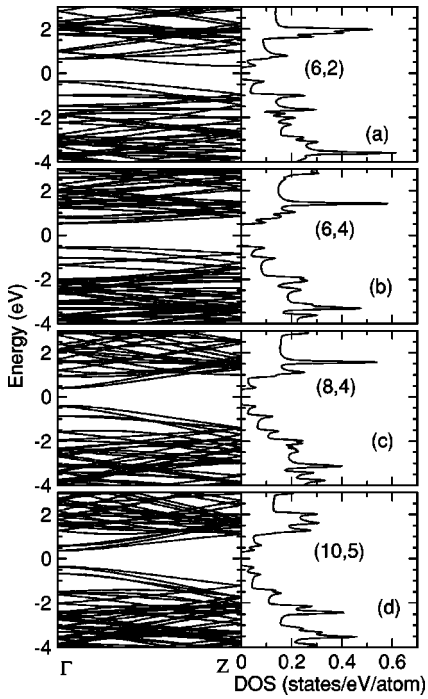

FIG. 6. Energy bands and density of states of the chiral nanotubes. The Fermi level is at 0 eV.

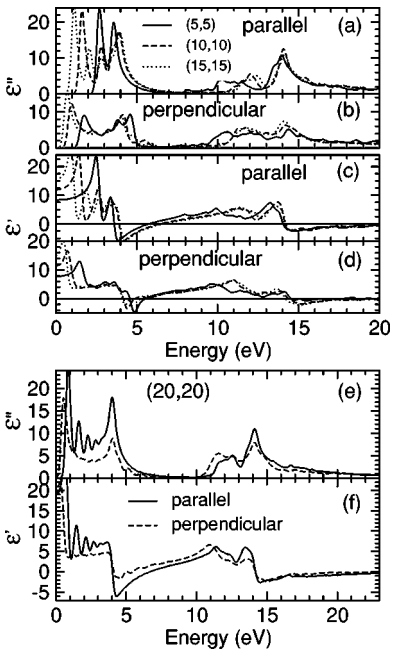

FIG. 7. Calculated dielectric function of the armchair nanotubes. Parallel and perpendicular denote electric fields polarized parallel and perpendicular to the nanotube axis, respectively.

energy range from 0 to 8 eV and the high-energy range from 8 to 20 eV. For $E\|\hat{z}$, the ε'' in the low-energy region consists of a few distinct peaks (Figs. 7–9 and Table III). These distinct features are especially pronounced for the semiconducting chiral nanotubes (Fig. 9) and can perhaps be used to characterize the chirality of the grown carbon nanotubes by optical means,[14,15,20,21] an important issue in the current nanotube research. For $E\perp\hat{z}$, in contrast, the ε'' spectrum in the low-energy region is made up of a dull broad hump (Figs. 7–9). The magnitude of the humps is considerably smaller than that of the peaks (Fig. 10).

The absorptive bandwidth gets wider as the diameter of the nanotube becomes larger. For the (20,20) nanotube the

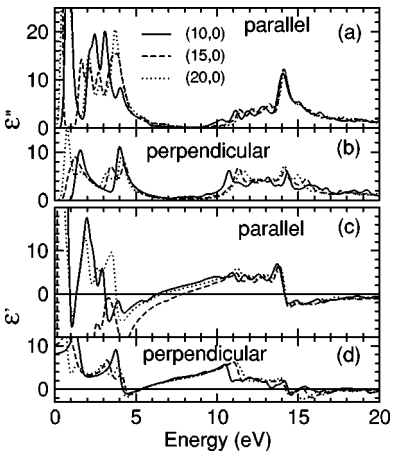

FIG. 8. Calculated dielectric function of the zigzag nanotubes. Parallel and perpendicular denote electric fields polarized parallel and perpendicular to the nanotube axis, respectively.

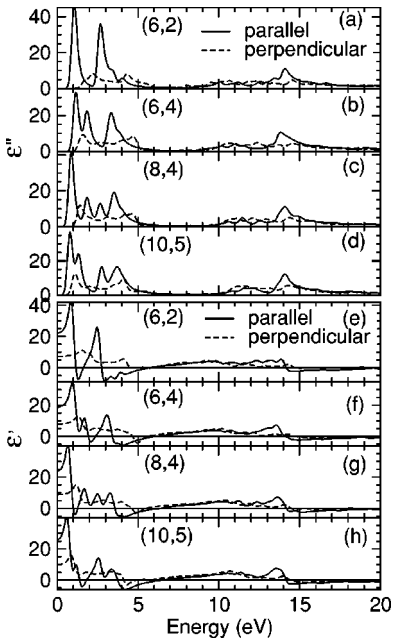

FIG. 9. Energy bands and density of states of the chiral nanotubes. The Fermi level is at 0 eV.

entire ε'' spectrum [Fig. 7(e)] becomes very similar to that of $E\perp c$ of graphite [Fig. 1(a)]. It appears that the optical anisotropy becomes smaller as the diameter becomes larger. In particular, for the (20,20) nanotube, the optical anisotropy is already small (Fig. 7). This perhaps can be explained as follows. For the large diameter nanotubes such as the (20,20) nanotube, the curvature effects are negligible and the band structure can be regarded as that obtained by the zone folding of the graphene sheet. As a result, the dielectric function for $E\|\hat{z}$ should be almost identical to that of $E\perp c$ of graphite. However, as mentioned before, the dielectric function for $E\perp\hat{z}$ is a uniform mixture of the dielectric functions of graphite for both $E\perp c$ and $E\|c$. Now the ε'' of graphite for $E\|c$ in the low-energy region is almost zero while in the high-energy the optical anisotropy of graphite is not large (Fig. 1). This results in small optical anisotropy in the large diameter carbon nanotubes such as the (20,20) nanotube

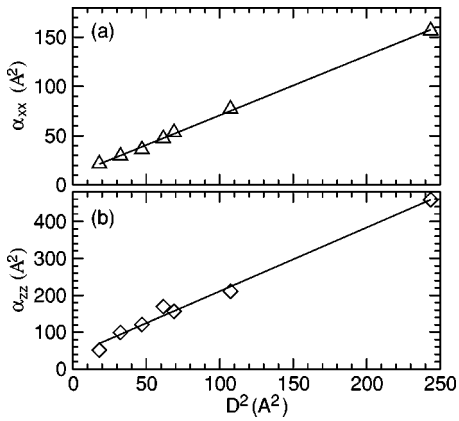

FIG. 10. (a) $\alpha_{xx}(0)$ and (b) $\alpha_{zz}(0)$ vs D^2 for the nanotubes studied. The solid line is a linear least-squares fit.

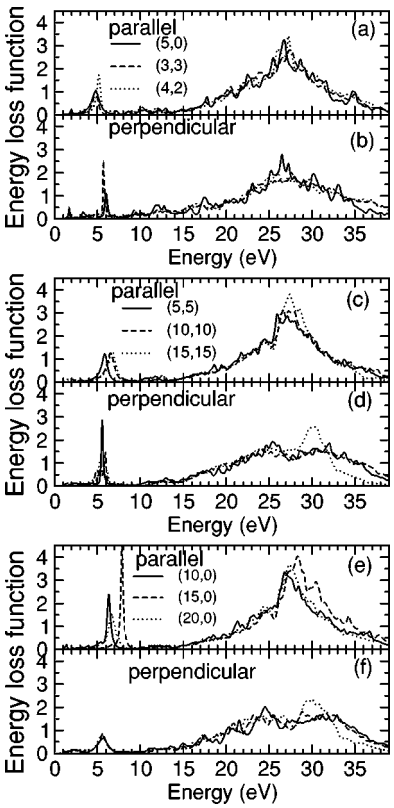

FIG. 11. Calculated energy loss function of the carbon nanotubes studied. Parallel and perpendicular denote electric fields polarized parallel and perpendicular to the nanotube axis, respectively.

(Fig. 6). Nevertheless, in optical experiments, one still expects to see a strong optical anisotropy because the ε'' spectrum for $E\perp\hat{z}$ would be substantially reduced due to the depolarization effect mentioned above.

The static values of the dielectric constant and electric polarizability of the semiconducting nanotubes are listed in Table III. Clearly, both quantities are highly anisotropic. In experiments, this anisotropy would be enhanced because the calculated $\varepsilon(0)$ and $\alpha(0)$ for $E\perp\hat{z}$ would be significantly reduced due to the depolarization effect.[31] Interestingly, $\alpha(0)$ per unit length for both electric-field polarizations is roughly proportional to D^2 (Fig. 10), i.e., $\alpha(0)=a_0+a_1D^2$, being independent of chirality and electronic structure. For $E\perp\hat{z}$, $a_0=10.1$ Å^2 and $a_1=0.61$ and for $E\|\hat{z}$, $a_0=38.0$ Å^2 and $a_1=1.73$. This behavior of $\alpha(0)$ can be understood in an empty lattice model of electrons moving freely on a cylinder of infinitesimal thickness.[33] Note that previous calculations based on a simple tight-binding model suggest that $\alpha(0)$ for $E\|\hat{z}$ is proportional to D/E_g^2.[31] We find that the present results of $\alpha_{zz}(0)$ do not follow this relation at all.

E. Electron energy loss spectrum

Shown in Fig. 11 are the calculated electron energy loss spectra (EELS) for the 4-Å nanotubes, the armchair nanotubes, and the zigzag nanotubes. Interestingly, for $E\|\hat{z}$, the EELS for all the nanotubes are similar to that of $E\perp c$ of graphite [Fig. 1(c)], being dominated by a broad $\pi+\sigma$-electron plasmon peak at 27 eV and a small π-electron plasmon peak at about 5–7 eV. The energy position of the low-energy peak is smaller than that of graphite (7 eV) except that (7.9 eV) of the (15,0) nanotube. The EELS hardly show any chirality dependence except that the energy position of the low-energy peak varies slightly as one goes from one nanotube to another. Interestingly, for the armchair nanotubes, as the diameter of the nanotube become larger, the energy position of the low-energy peak rapidly approachs that of graphite, being 5.9 eV for (5,5), 6.6 eV for (10,10), and 6.8 eV for (15,15) [Figs. 11(c) and 11(d)]. In contrast, for the zigzag nanotubes, the energy position of the low-energy peak oscillates, being 6.3 eV for (10,0), 7.9 eV for (15,0), and 6.7 eV for (20,0) [Figs. 11(e) and 11(f)].

Unlike the case of $E\|c$ of graphite [Fig. 1(c)], the EELS for $E\perp\hat{z}$ is very similar to that of $E\|\hat{z}$ in shape but somewhat smaller in amplitude. A rather pronounced difference is the energy position of the π-electron plasmon peak [Fig. 1(c)]. The weak anisotropy in the EELS of the nanotubes may be attributed to the fact that for $E\perp\hat{z}$ all the $\pi\rightarrow\pi^*$, $\sigma\rightarrow\sigma^*$, $\pi\rightarrow\sigma^*$, and $\sigma\rightarrow\pi^*$ optical transitions are excited while in graphite only $\pi\rightarrow\pi^*$ and $\sigma\rightarrow\sigma^*$ transitions are possible for $E\|c$.

The EELS of the chiral [(6,2), (6,4), (8,4), and (10,5)] nanotubes have also been calculated. However, the EELS are similar to that of the armchair and zigzag nanotubes, and therefore, they are not shown here. Like the armchair nanotubes, the energy position of the low-energy peak rapidly approaches that of graphite, being 5.8 eV for (6,2), 6.1 eV for (6,4), 6.4 eV for (8,4), and 6.5 eV for (10,5).

F. Second-order optical susceptibility

Unlike armchair and zigzag nanotubes, the chiral nanotubes would exhibit second-order nonlinear optical behavior. In Fig. 12, the calculated real and imaginary parts of the second-order optical susceptibility $\chi^{(2)}_{xyz}(-2\omega,\omega,\omega)$ for all the five chiral nanotubes [(4,2), (6,2), (6,4), (8,4), and (10,5)] are displayed. The corresponding absolute values of $\chi^{(2)}_{xyz}(-2\omega,\omega,\omega)$ are displayed in Fig. 13. Because of one-dimensional chiral symmetry, only two elements out of the eighteen elements of the second-order susceptibility tensor are nonzero. These two nonzero elements are $\chi^{(2)}_{xyz}$ and $\chi^{(2)}_{yzx}$. Furthermore, both the real and imaginary parts of these two elements have the same values but opposite signs, i.e., $\chi^{(2)}_{xyz}=-\chi^{(2)}_{yzx}$. Therefore, only $\chi^{(2)}_{xyz}$ are shown here. Furthermore, the static values of $\chi^{(2)}_{xyz}$ and $\chi^{(2)}_{yzx}$ are zero, as required by the so-called Kleinman symmetry[34] which demands $\chi^{(2)}_{xyz}(0)=\chi^{(2)}_{yzx}(0)$.

Figure 12 shows that for all the chiral nanotubes studied here, both the real and imaginary parts of $\chi^{(2)}_{xyz}(-2\omega,\omega,\omega)$ show an oscillatory behavior. The amplitude of these oscillatory real and imaginary parts is very large in the photon energies of 0.1–4.0 eV. Indeed, the absolute value of $\chi^{(2)}_{xyz}(-2\omega,\omega,\omega)$ for all the chiral nanotubes in this photon energy range is huge (see Fig. 13). For example, the absolute

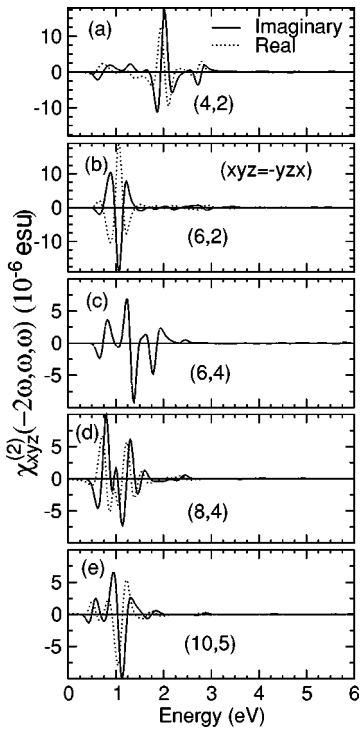

FIG. 12. Real and imaginary parts of $\chi^{(2)}_{xyz}(-2\omega,\omega,\omega)$ of the chiral nanotubes.

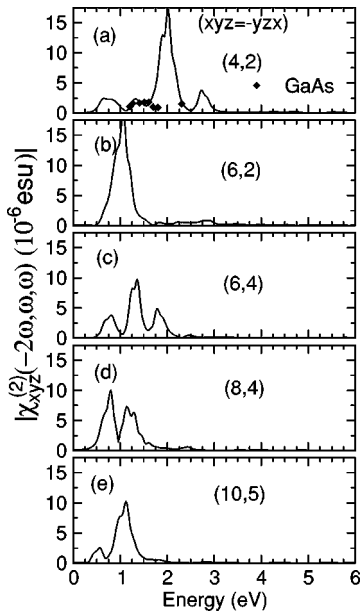

FIG. 13. Absolute value of $\chi^{(2)}_{xyz}(-2\omega,\omega,\omega)$ of chiral nanotubes. In (a), the measured $\chi^{(2)}$ values of GaAs are also plotted (diamonds).

value for the (4,2) and (6,2) nanotubes is around 15 $\times 10^{-6}$ esu at 2 and 1 eV, respectively. These values are nearly ten times larger than that of GaAs[35] (Fig. 13). Note that GaAs is among the semiconductors which possess the largest second-order optical susceptibilities. This suggests that small diameter chiral carbon nanotubes would be good nonlinear optical materials and have potential applications in the area of nonlinear optics, e.g., second-harmonic generation and sum-frequency generation. It is interesting to note that the absolute value of $\chi^{(2)}_{xyz}(-2\omega,\omega,\omega)$ becomes smaller as one goes from the (4,2) and (6,2) nanotubes to the (6,4) and (8,4) nanotubes and to the (10,5) nanotube. This may be expected because the diameter of the nanotube becomes larger as one goes along the series of (4,2), (6,2), (6,4), (8,4), and (10,5) (see Table I). Now since when the radius of a nanotube is very large, the properties of the nanotube will approach that of a graphene sheet (or graphite) which has zero second-order optical susceptibility.

IV. SUMMARY

Summarizing, we have carried out a systematic *ab initio* study of the optical as well as structural and electronic properties of the CNT's within density-functional theory in the local-density approximation. Highly accurate PAW method was used and calculation of the optical properties was based on the independent-particle approximation. Specifically, the properties of the armchair [(3,3),(5,5),(10,10),(15,15), (20,20)], zigzag [(5,0),(10,0), (15,0),(20,0)], and chiral [(4,2),(6,2),(6,4),(8,4),(10,5)] nanotubes have been calculated. For comparison, the structural, electronic, and optical properties of graphite and the graphene sheet have also been calculated. We find that the calculated structural and optical properties of graphite are in good agreement with experiments. Furthermore, the calculated band gap of the (15,0) nanotube is in good agreement with recent STM measurements.[32] The calculated energy positions of the absorption peaks in the 4-Å nanotubes also agree reasonable well with the corresponding measured values (within 15%). This suggests that the present theoretical approach is perhaps adequate for investigating the optical properties of the carbon nanotubes.

We find that like graphite, the optical properties of the nanotubes can be divided into two spectral regions, namely, the low-energy region (0–8 eV) in which optical transitions involve mainly the π bands and the high-energy region (8–25 eV) where interband transitions involve mainly the σ bands. Interestingly, for the electric-field vector polarized parallel to the nanotube axis, the absorptive part ε'' of the optical dielectric function for the small nanotubes (the diameter being smaller than, say, 25 Å) in the low-energy region consists of a few distinct peaks. Furthermore, the energy position, the shape, and the number of the peaks depend rather strongly on the diameter and chirality. This suggests that one could use these distinct optical features to characterize the chirality and diameter of the grown nanotubes, as has been demonstrated recently.[15] In contrast, for the electric-field vector polarized perpendicular to the nanotube axis, the ε'' spectrum of all the nanotubes studied except the three 4 Å nanotubes in the low-energy region is made up of a broad hump. The bandwidth of the hump increases with the nanotube diameter and the magnitude of the hump is in general about half of that of the ε'' for the electric-field vector polarized parallel to the nanotube axis. Surprisingly, given their one-dimensional character, the optical anisotropy of the

nanotubes is smaller than that of graphite. Moreover, the larger the diameter, the smaller the optical anisotropy. For the nanotubes with a moderate diameter (say, 30 Å) such as the (20,20) nanotube, the optical anisotropy is not large and the ε'' spectrum for both electric-field polarizations becomes rather similar to that of graphite with electric-field polarization parallel to the graphene layers. Nevertheless, one would still see a strong anisotropy in optical experiments because the calculated ε'' for $E \perp \hat{z}$ would be significantly reduced due to the depolarization effect.

The calculated static polarizability $\alpha(0)$ for the semiconducting nanotubes is rather anisotropic with $\alpha_{zz}(0)$ being several times larger than $\alpha_{zz}(0)$. For both electric-field polarizations, $\alpha(0)$ is nearly proportional to the square of the tube diameter, being independent of chirality and electronic structure.

The calculated electron energy loss spectra of all the nanotubes studied here for both electric-field polarizations are similar to that of $E \perp c$ of graphite, being dominated by a broad $\pi+\sigma$-electron plasmon peak at near 27 eV and a small π-electron plasmon peak at $5 \sim 7$ eV. The energy position of the low-energy peak rapidly approaches that of graphite as the diameter of the nanotube increases. Thus, the anisotropy is much smaller than that of graphite.

Only the chiral nanotubes would exhibit second-order nonlinear optical behavior. Two elements (χ^2_{xyz} and χ^2_{yzx}) of the second-order susceptibility tensor are nonzero, and they have the same values but opposite signs. For all the chiral nanotubes studied here, both the real and imaginary parts of $\chi^{(2)}_{xyz}(-2\omega,\omega,\omega)$ show an oscillatory behavior. The absolute value of $\chi^{(2)}_{xyz}(-2\omega,\omega,\omega)$ of all the chiral nanotubes in the optical energy range of 0.1–3.0 eV is huge, being up to ten times larger than that of GaAs. This suggests that small diamter chiral carbon nanotubes could have potential applications in nonlinear optics, e.g., second-harmonic generation and sum-frequency generation. However, the absolute value of $\chi^{(2)}_{xyz}(-2\omega,\omega,\omega)$ becomes smaller as the nanotube diameter increases. This may be attributed to the fact that when the diameter of a nanotube is very large, the properties of the nanotube will approach that of a graphene sheet which has zero second-order optical susceptibility. Furthermore, the static value of both $\chi^{(2)}_{xyz}$ and $\chi^{(2)}_{yzx}$ is zero, satisfying the Kleinman symmetry.

ACKNOWLEDGMENTS

The authors acknowledge financial support from National Science Council of Taiwan (NSC Grant No. 92-2120-M002-003), Ministry of Education of Taiwan, and Ministry of Economic Affairs of Taiwan (Grant No. 92-EC-17-A-08-S1-0006).

*Electronic address: gyguo@phys.ntu.edu.tw

[1] S. Iijima, Nature (London) **354**, 56 (1991).
[2] M. Bockrath, D.H. Cobden, J. Lu, A.G. Rinzler, R.E. Smalley, L. Balents, and P.L. McEuen, Nature (London) **397**, 598 (1999).
[3] M.F. Lin and D.S. Chuu, Phys. Rev. B **57**, 6731 (1998).
[4] L. Liu, G.Y. Guo, C.S. Jayanthi, and S.Y. Wu, Phys. Rev. Lett. **88**, 217206 (2002).
[5] R. Saito, G. Dresselhaus, and M. S. Dresselhaus, *Physical Properties of Carbon Nanotubes* (Imperial College, London, 1998).
[6] S. Tasaki, K. Maekawa, and T. Yamabe, Phys. Rev. B **57**, 9301 (1998).
[7] I. Bozovic, N. Bozovic, and M. Damnjanovic, Phys. Rev. B **62**, 6971 (2000).
[8] O.E. Alon, V. Averbukh, and N. Moiseyev, Phys. Rev. Lett. **85**, 5218 (2000).
[9] E.L. Ivchenko and B. Spivak, Phys. Rev. B **66**, 155404 (2002).
[10] W.A. de Heer, W.S. Bacsa, A. Chatelain, T. Gerfin, R. Humphrey-Baker, L. Forro, and D. Ugarte, Science **268**, 845 (1995).
[11] R. Kuzuo, M. Terauchi, and M. Tanaka, Jpn. J. Appl. Phys., Part 2 **31**, L1484 (1992); V.P. Dravid, X. Lin, Y. Wang, A. Lee, J.B. Ketterson, and R.P.H. Chang, Science **259**, 1601 (1993); P.M. Ajayan, S. Iijima, and T. Ichihashi, Phys. Rev. B **47**, 6859 (1993); L.A. Bursill, P.A. Stadelmann, J.L. Peng, and S. Prawer, *ibid.* **49**, 2882 (1994).
[12] F. Bommeli, L. Degiorgi, P. Wachter, W.S. Bacsa, W.A. de Heer, and L. Forro, Solid State Commun. **99**, 513 (1996).
[13] M. Ichida, S. Mizuno, Y. Tani, Y. Saito, and A. Nakamura, J. Phys. Soc. Jpn. **68**, 3131 (1999).
[14] Z.M. Li, Z.K. Tang, H.J. Liu, N. Wang, C.T. Chan, R. Saito, S. Okada, G.D. Li, J.S. Chen, N. Nagasawa, and S. Tsuda, Phys. Rev. Lett. **87**, 127401 (2001).
[15] S.M. Bachilo, M.S. Strano, C. Kittrell, R.H. Hauge, R.E. Smalley, and R.B. Wiesman, Science **298**, 2361 (2002).
[16] H. Ajiki and T. Ando, Physica B **201**, 349 (1994); Jpn. J. Appl. Phys., Suppl. **34**, 107 (1995).
[17] M.F. Lin and Kenneth W.-K. Shung, Phys. Rev. B **50**, 17 744 (1994).
[18] X. Wan, J. Dong, and D.Y. Xing, Phys. Rev. B **58**, 6756 (1998).
[19] J. Jiang, J. Dong, and D.Y. Xing, Phys. Rev. B **59**, 9838 (1999).
[20] H.J. Liu and C.T. Chan, Phys. Rev. B **66**, 115416 (2002).
[21] M. Machon, S. Reich, C. Thomsen, D. Sanchez-Portal, and P. Ordejon, Phys. Rev. B **66**, 155410 (2002).
[22] P.E. Blöchl, Phys. Rev. B **50**, 17 953 (1994); G. Kresse and D. Joubert, *ibid.* **59**, 1758 (1999).
[23] G. Kresse and J. Hafner, Phys. Rev. B **47**, 558 (1993); **49**, 14 251 (1994); G. Kresse and J. Furthmüller, Comput. Mater. Sci. **6**, 15 (1996).
[24] R. Ahuja, S. Auluck, J.M. Wills, M. Alouani, B. Johansson, and O. Eriksson, Phys. Rev. B **55**, 4999 (1997).
[25] J. Li, C.-G. Duan, Z.-Q. Gu, and D.-S. Wang, Phys. Rev. B **57**, 2222 (1998).
[26] B. Adolph, J. Furthmüller, and F. Bechstedt, Phys. Rev. B **63**, 125108 (2001).
[27] C.-G. Duan, J. Li, Z.-Q. Gu, and D.-S. Wang, Phys. Rev. B **60**, 9435 (1999).
[28] Ed. Ghahramani, D.J. Moss, and J.E. Sipe, Phys. Rev. Lett. **64**, 2815 (1990); Phys. Rev. B **43**, 8990 (1991).
[29] R. Klucker, M. Skibowski, and W. Steinmann, Phys. Status Solidi B **65**, 703 (1974).

[30] E.A. Taft and H.R. Philipp, Phys. Rev. **138**, A197 (1965).
[31] L.X. Benedict, S.G. Louie, and M.L. Cohen, Phys. Rev. B **52**, 8541 (1995).
[32] M. Ouyang, J.-L. Huang, C.-L. Cheung, and C.M. Lieber, Science **292**, 702 (2001).
[33] M.F. Lin and Kenneth W.-K. Shung, Phys. Rev. B **47**, 6617 (1993).
[34] D.A. Kleinmam, Phys. Rev. **126**, 1977 (1962).
[35] R.K. Chang, J. Ducuing, and N. Bloembergen, Phys. Rev. Lett. **15**, 415 (1965).